Talanta 299 (2026) 129054

Contents lists available at ScienceDirect

Talanta

journal homepage: www.elsevier.com/locate/talanta

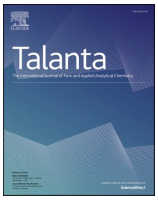

Truncated PNA-functionalized porous silicon biosensor for low-cost and early detection of troponin T in myocardial infarction

Maria Grazia Nolli [a,1], Alessio Bartocci [b,1], Caterina De Rosa [c,1], Andrea Patrizia Falanga [a], Vincenzo Abbate [d], Monica Terracciano [a,*], Valeria Nocerino [e,f], Ilaria Rea [f,**], Luca De Stefano [f], Sabrina Giordano [a], Gennaro Piccialli [a,g], Marco Fabio Costantino [h], Carminia Maria Della Corte [c], Elise Dumont [i,j], Nicola Borbone [a,g], Giovanni Orabona Dell'Aversana [d], Giorgia Oliviero [g,k,***]

[a] *Department of Pharmacy, University of Naples Federico II, via Domenico Montesano 49, 80131, Naples, Italy*
[b] *Department of Medical Biotechnology and Translational Medicine, University of Milan, Via Fratelli Cervi 93, 20054, Segrate, MI, Italy*
[c] *Department of Precision Medicine, University of Campania Luigi Vanvitelli, Via Sergio Pansini 5, 80131, Naples, Italy*
[d] *Maxillofacial Surgery Unit, Department of Neurosciences, Reproductive, and Odontostomatological Sciences, University of Naples Federico II, Via Sergio Pansini 5, 80131, Naples, Italy*
[e] *Department of Electrical Engineering and Information Technology, University of Naples Federico II, Via Claudio 21, 80125, Naples, Italy*
[f] *Institute of Applied Sciences and Intelligent Systems (ISASI) Naples Unit-National Research Council, Via Pietro Castellino 111, 80131, Naples, Italy*
[g] *ISBE-IT, University of Naples Federico II, Corso Umberto I 40, 80138, Naples, Italy*
[h] *Cardiovascular Department, Institute of Cardiology, San Carlo Hospital, Via Potito Petrone, 85100, Potenza, Italy*
[i] *Université Côte d'Azur, CNRS, Institut de Chimie de Nice, UMR 7272, 06108, Nice, France*
[j] *Institut Universitaire de France, 5 rue Descartes, 75005, Paris, France*
[k] *Department of Molecular Medicines and Medical Biotechnologies, University of Naples Federico II, via Sergio Pansini 5, 80131, Naples, Italy*

ARTICLE INFO

Keywords:
In silico study
PNA bio-probe
PSi optical transducer
Surface chemical functionalization
Label-free cardiac troponin T detection

ABSTRACT

A label-free optical biosensor based on porous silicon (PSi) was developed for the high-sensitivity detection of human cardiac troponin T (cTnT), a key biomarker for the early diagnosis of myocardial infarction (MI). To reduce synthesis costs while maintaining binding efficiency, a truncated peptide nucleic acid (PNA) probe was designed *in silico* starting from a 40-base-long wild-type sequence. Computational screening identified a 12-base candidate, whose binding affinity was experimentally validated by Western blot analysis. The freshly etched PSi surface was passivated and functionalized via mild thermal hydrosilylation with 10-undecenoic acid to introduce carboxylic groups, enabling covalent PNA immobilization through the carbodiimide chemistry. Surface functionalization and stability in aqueous media were validated using both label-free optical reflectance and fluorescence spectroscopy. Probe conjugation was optimized at pH 5.5, resulting in a surface density of 1.12 ± 0.30 pmol cm^{-2}. The biosensor exhibited reproducible, concentration-dependent responses to cTnT in the 0.02–0.16 ng mL^{-1} range, with a limit of detection of $0.030 \pm 2.0 \times 1\ 0^{-5}$ ng mL^{-1}. This performance is clinically relevant, as cTnT levels in healthy individuals are typically <0.01 ng mL^{-1}, while MI patients often exceed 10 ng mL^{-1}, reaching >100 ng mL^{-1} in severe cases.

1. Introduction

Myocardial infarction (MI) is a leading cause of global mortality and a major contributor to emergency department visits, significantly exacerbating overcrowding [1,2]. Timely diagnosis is critical to reduce mortality rates and prevent irreversible cardiac tissue damage. However, conventional diagnostic methods, such as ELISA assays for cardiac troponin detection, require centralized laboratories, specialized

---

* Corresponding author.
** Corresponding author.
*** Corresponding author. ISBE-IT, University of Naples Federico II, Corso Umberto I 40, 80138, Naples, Italy.

E-mail addresses: monica.terracciano@unina.it (M. Terracciano), ilaria.rea@na.isasi.cnr.it (I. Rea), giorgia.oliviero@unina.it (G. Oliviero).

[1] These authors contributed equally to this work.

https://doi.org/10.1016/j.talanta.2025.129054
Received 2 September 2025; Received in revised form 15 October 2025; Accepted 28 October 2025

personnel, and long response times, significantly delaying clinical triage and limiting, in some cases, timely therapeutic intervention [3,4]. In this context, point-of-care (PoC) devices provide a promising solution for rapid and accurate diagnosis, helping to alleviate the hospital burden, particularly in cases of false alarms, and enabling decentralized testing outside traditional clinical settings [5]. The COVID-19 pandemic further underscored the importance of rapid diagnostic tools for large-scale emergency management [6–8]. Nevertheless, the adoption of PoC tests for MI remains limited, mainly due to high production and implementation costs [9]. Developing affordable and accessible diagnostic devices could significantly improve emergency department efficiency, support decentralized care models, and ensure timely treatment for patients [10]. This study presents the design and proof-of-concept development of a low-cost, label-free biosensing platform for the detection of human cardiac troponin T (cTnT) as a model biomarker of MI. High-sensitivity cardiac troponins (cTnT and cTnI) are currently recognized as the most specific and sensitive biomarkers for detecting myocardial injury and diagnosing MI, reflecting the release of structural proteins unique to cardiomyocytes and strongly associated with myocardial damage [11–13]. The troponin complex consists of three regulatory proteins, troponin C (cTnC), troponin I (cTnI), and troponin T (cTnT), that mediate calcium-dependent muscle contraction. The cardiac-specific isoforms of cTnI and cTnT are structurally distinct from their skeletal counterparts, enabling selective detection of myocardial injury [14,15]. During MI, both proteins are released into circulation as a mixture of intact, truncated, and complex-bound isoforms due to proteolytic degradation processes. The true elimination half-life of the intact forms has been estimated to be a few hours, although circulating levels may remain elevated for an extended period as a result of continuous myocardial release [13,14].

In particular, cTnT shows extremely low serum concentrations in healthy individuals (<0.01 ng mL^{-1}) but rises sharply after myocardial injury, often exceeding 10 ng mL^{-1} and reaching >100 ng mL^{-1} in severe infarction [16].

Although some analytical differences between cTnT and cTnI have been reported, modern high-sensitivity assays provide comparable clinical performance, and both biomarkers offer complementary diagnostic information depending on the clinical context [11,15,17].

In this proof-of-concept study, full-length cTnT was selected as a model biomarker owing to its structural complexity, the availability of well-characterized binding sequences, and its ready accessibility as a purified reference analyte, facilitating probe design and analytical validation.

However, one of the main challenges in designing biosensors is the selection of the bioprobe, which must be specific, stable, and low-cost. Conventional bioprobes, such as antibodies and DNA-based probes, have limitations related to denaturation, variability, high-cost production, and susceptibility to enzymatic degradation, reducing their effectiveness in real diagnostic settings [18].

To overcome these issues, interest in synthetic analogs of oligonucleotides, such as Peptide Nucleic Acids (PNAs), has recently increased [19–21]. PNAs are DNA mimics with a pseudo-peptidic backbone that provides greater stability and resistance to enzymatic degradation [22]. Moreover, their high affinity for complementary DNA or RNA sequences makes them particularly suitable for recognizing protein-based biomarkers like cTnT [23–25]. However, the high cost of synthesis, particularly for longer sequences, poses significant challenges for the application of these probes in low-cost diagnostic devices [26].

Here, a truncation strategy was applied to wild-type 40-mer sequences previously reported to exhibit high affinity for cardiac troponins, preserving key base pairs necessary for target recognition [27,28]. Four truncated sequences were selected: PNA-1 (6 bases), PNA-2 (8 bases), PNA-3 (12 bases), and PNA-4 (16 bases), synthesized in both unmodified and N-terminally acetylated forms to evaluate the impact of acetylation on binding performance. Additionally, four lysine (Lys) residues were introduced at the C-terminus of each sequence to enhance water solubility and stability under physiological conditions [29].

The binding capabilities of the truncated PNAs were initially assessed through computational prediction and subsequently validated by Western blot analysis to confirm the affinity and specificity toward cTnT [30]. The truncated sequence with binding affinity closest to that of the wild-type was selected for biosensor fabrication.

Porous silicon (PSi) was selected as the transducer material for the label-free optical biosensor due to its high surface area, simple fabrication through electrochemical etching, and low production cost [31]. However, the intrinsic instability of freshly etched PSi remains a major limitation for its use in biosensing applications [32,33]. To address this issue, a hydrosilylation strategy using 10-undecenoic acid was employed, reducing reaction times and enabling milder conditions compared to conventional methods [32]. This treatment replaced unstable Si–H bonds with stable Si–C bonds while introducing carboxyl (COOH) groups to enable efficient bioprobe conjugation [32,34].

The selected PNA probe was immobilized onto the PSi surface via carbodiimide (EDC/NHS) chemistry, optimizing the pH conditions to achieve efficient bioconjugation [25]. Stability test of both the passivated transducer and the complete PNA-based biosensor was performed under physiological conditions. Subsequently, the biosensor performance was evaluated by detecting increasing concentrations of cTnT (0.02, 0.04, 0.08, and 0.16 ng mL^{-1}) to determine sensitivity and the detection limit. Each functionalization step and sensing measurement was monitored by reflectometric interference spectroscopy, a label-free optical technique sensitive to refractive index changes caused by the infiltration of organic material into the porous matrix.

2. Materials and Methods

2.1. Chemicals

10-Undecenoic acid (UDA), ethylaluminum dichloride ($EtAlCl_2$), 2-(*N*-morpholino)ethanesulfonic acid (MES) hydrate, hydrofluoric acid (HF), 1-ethyl-3-(3-dimethylaminopropyl)carbodiimide hydrochloride (EDC), *N*-hydroxysuccinimide (NHS), Protein A-FITC (PrA*), tetrahydrofuran (THF), isopropanol (IPA), trifluoroacetic acid (TFA), acetonitrile, anhydrous toluene, phosphate buffered saline (PBS 1 ×), ethanol, formic acid, sodium hydroxide and water were purchased from Sigma Aldrich (St. Louis, MO, USA). PNA monomers were purchased from Link Technologies (Bellshill, Lanarkshire, UK). Fmoc-L-Lys(MMT)-OH was purchased from Iris Biotech GmbH (Marktredwitz, Germany). All solvents for synthesizing PNA molecules and 4-methylbenzhydrylamine (MBHA) resin (1 % divinylbenzene, 200–400 mesh, 0.5 mmol g^{-1} loading) were purchased from Sigma-Aldrich.

2.2. PNA synthesis, purification, and analysis

PNAs obtained through wild-type sequence reduction (PNA-1, PNA-2, PNA-3, and PNA-4) and control PNA (ctrl PNA) (Table 1) were synthesized on a Biotage Initiator Alstra microwave-assisted peptide synthesizer (Biotage Sweden AB, Uppsala, Sweden) using the 9-fluorenylmethoxycarbonyl (Fmoc) solid-phase strategy. Initially, 150 mg of MBHA resin underwent swelling in dimethylformamide (DMF) overnight. Subsequently, the Fmoc protecting groups were removed after treatment with a solution of 20 % (v/v) piperidine in DMF for 10

Table 1
PNA sequences synthesized by solid-phase strategy.

Sample	Sequence
PNA-1	H_2N-gctgcc-$(Lys)_4$-$CONH_2$
PNA-2	CH_3COHN-cagctgcc-$(Lys)_4$-$CONH_2$
PNA-3	H_2N-ctgcccctctta-$(Lys)_4$-$CONH_2$
PNA-4	CH_3COHN-gcacctgcccctctta-$(Lys)_4$-$CONH_2$
ctrl PNA	H_2N-tttttttttttt-$(Lys)_4$-$CONH_2$

min. After DMF washes, four lysine couplings were carried out using Fmoc-L-Lys(MMt)-OH (MMt = monomethoxytrityl) under the following conditions: 4 equiv. of a 0.2 mol L^{-1} solution of Fmoc-L-Lys (MMt)-OH monomer in DMF, 4 equiv. of a 0.2 mol L^{-1} solution of hexafluorophosphate azabenzotriazole tetramethyl uronium (HATU) in DMF, 4 equiv. of *N*,*N*-diisopropylethylamine (DIPEA), and 6 equiv. of lutidine for 40 min at room temperature (RT). PNA monomers were then introduced using the same synthesis conditions. After each coupling step, a capping with acetic anhydride in the presence of DIPEA was performed for 10 min at RT, followed by removal of the Fmoc group through two treatments with a solution of 20 % piperidine in DMF for 10 min. At the conclusion of the synthetic cycle, the PNAs were detached from the solid support by treatment with TFA/triisopropylsilane (TIS)/H_2O (9.5:0.25:0.25; v/v/v) for 2 h, and the products were precipitated with cold diethyl ether and recovered by centrifugation. The residual ether was removed by evaporation under nitrogen gas. The precipitates were then dissolved in water and finally lyophilized. The crude samples underwent purification through semipreparative HPLC analyses on a Jasco HPLC system (Jasco Europe S.r.l., Cremella, Italy), utilizing a Macherey-Nagel (Düren, Germany) 10 × 250 mm C-18 reverse-phase column (particle size 5 μm). Elution was carried out with a linear gradient of acetonitrile containing 0.1 % (v/v) TFA in water (from 0 to 100 % acetonitrile in 30 min, flow rate 3 mL min^{-1}). Subsequently, the collected fractions were lyophilized, and the quantity of each PNA dissolved in pure water was estimated through quantitative UV with a Jasco V-530 spectrophotometer (λ = 220–320 nm, 400 nm min^{-1} scanning speed, 2.0 nm bandwidth) at 260 nm and 90 °C using the molar extinction coefficient ε = 100 200 L cm^{-1} mol^{-1} for PNA and ε = 105 600 L cm^{-1} mol^{-1} for ctrl PNA, calculated using PNA Tool (https://www.pnabio.com/support/PNA_Tool.htm). The final PNA products were characterized by ESI-MS on an ABSciex 4000 Q TRAP mass spectrometer (ThermoFisher Scientific, Waltham, MA, USA) operating in positive ion mode by preparing 20 μmol L^{-1} PNA stock solutions containing 0.1 % (v/v) formic acid in water (see Fig. S1–S11) [25].

2.3. *In silico studies*

Model Preparation. cTnT monomer structure was extracted from troponin complex cTnI-cTnX-cTnT (PDB ID: 1J1D). Missing residues on the two helices were reconstructed with alphafold3 [35]. The protonation state of protein titratable residues was determined via the H++ server (http://newbiophysics.cs.vt.edu/H++) at the experimental pH of 7.0. PNA sequences were obtained using tleap tool of Ambertools [36]. The linear sequences, embedded within a box of water and ions, were relaxed by Molecular Dynamics simulations (MDs) to generate representative starting structures. The first most relevant structure obtained by cluster analysis was then used for molecular docking with the protein (see section “Molecular Dynamics Setup” of SI).

Troponin-PNA Molecular Docking. Given the complexity and the multi-basin surface for cTnT-PNA recognition process, we relied on molecular blind docking to obtain starting structures for the cTnT-PNA complex. The docking was performed using the HDOCK web server, a docking approach based on biochemical or biophysical information [37], treating the cTnT as the receptor and the PNA sequences as ligands. We were confident that this approach could yield useful results, as it has been previously benchmarked for computational studies on troponin-aptamers [38]. Among all the structures obtained by molecular docking, the lowest-energy one (HDOCK score) was then used as a starting point for MDs [39].

Force Field Parameters and MD Simulation Protocol. cTnT protein was treated using the AMBER ff14SB force field [40], while for PNA molecules Sanders et al. parameters were used [41]. Classical all-atom MDs were performed using the Amber22 package [36]. Details on the setup of simulation boxes are given in the section “Molecular Dynamics Setup” of SI. The systems, formed by cTnT-PNA complexes, solvated with TIP3P water molecules [42] and 0.150 mol L^{-1} NaCl, were initially minimized for 10 000 steps (5000 of steepest descent and 5000 of conjugate gradient) and then heated up from 0 to 300 K for a total of 30 ps in the isothermal–isochoric (NVT) ensemble with an integration time step of 1.0 fs. All during these phases, position restraints were applied on the protein and ligands’ heavy atoms, with a force constant of 5 kcal mol^{-1} $Å^{-2}$. Equilibration was then carried out for 1 ns in the isothermal–isobaric (NPT) ensemble with an integration timestep of 2 fs, and the position restraints force constant decreased to 2.5 kcal mol^{-1} $Å^{-2}$. A subsequent equilibration of 1 ns followed, with no position restraints applied. Temperature control was achieved using the Langevin thermostat (collision frequency (γcoll) of 1 ps^{-1}), while the pressure control in the NPT ensemble (P = 1 atm) was achieved using the Berendsen barostat [43]. Three subsequent production run replicates of 300 ns each, with different initial velocities, were launched, giving a total of 0.9 μs sampling time per system. During equilibration and production runs, the temperature was stabilized at 300 K and a cutoff of 10 Å was applied for the van der Waals electrostatic interactions and the real space of the electrostatic interaction. A slightly lower cutoff of 8 Å and 9 Å was used during the minimization and the heating processes, respectively. Long-range electrostatic interactions were computed using the particle mesh Ewald (PME) algorithm [44]. Post-process analysis was carried out throughout the production runs. All the bonds involving hydrogen were treated with the SHAKE constraints algorithm [45].

2.4. *Western blot analysis*

Human cardiac troponin T (cTnT, MW 37 kDa, Calbiochem, Nottingham, UK) 1 μg mL^{-1} alone or with PNAs was resuspended in RIPA buffer containing 0.1 % sodium dodecyl sulfate (SDS), 0.5 % sodium deoxycholate, 1 % Nonidet P-40, 100 mmol L^{-1} NaCl, 10 mmol L^{-1} Tris–HCl (pH 7.4), 0.5 mmol L^{-1} DTT, and 0.5 mmol L^{-1} PMSF. Each sample containing comparable amounts of protein was mixed and boiled at 100 °C for 5 min. Samples were resolved by SDS-PAGE gels and electrotransferred onto 0.2 μm nitrocellulose membranes (Trans-Blot Turbo; BioRad Laboratories, Hercules, CA, USA). After blocking membranes for 90 min at RT with 5 % non-fat dry milk TBS (Invitrogen, Thermo Fisher Scientific, Waltham, MA, USA), they were incubated overnight at 4 °C with mouse anti-troponin T monoclonal antibody (Sigma-Aldrich) and then with horseradish peroxidase-linked anti-mouse (BioRad Laboratories) for 1 h at RT. Detection of chemiluminescence reaction was performed with a Clarity Western ECL Substrate (BioRad Laboratories) using the ChemiDoc system (BioRad Laboratories). Images were analyzed using the BioRad Image Lab 3.0.1 software. The same protocol was used for the control protein Human Macrophage Migration Inhibitory Factor (MIF, MW 48 kDa, Sigma-Aldrich) and its corresponding Chicken Polyclonal MIF antibody (Abcam, Cambridge, UK). The Western blot signals were quantified by morpho-densitometric analysis using the ImageJ software version 1.53h17 (NIH, Bethesda, MD, USA) [46]. Briefly, the product of the area and optical density of each band was determined, and the relative protein level of each upper band was compared with that of the corresponding lower band. Data are expressed as the mean ± SD. The analysis was performed using the Prism 8 software (GraphPad Software, San Diego, CA, USA). Unpaired Student’s t-test with p-value <0.05 was considered to indicate statistical significance. All the experiments were repeated a minimum of three times independently to ensure reproducibility [47].

2.5. *Porous silicon fabrication and hydrosilylation process*

The single-layer PSi structure was obtained by electrochemical etching of n-type crystalline silicon (0.01–0.02 Ω cm resistivity, <100> orientation, 500 μm thickness) in 200 mL HF (5 % in weight)/ethanol solution at RT. The native oxide layer on the silicon substrate was removed by immersion in 10 mL HF (1 % in weight)/ethanol solution for a few minutes before the etching process. A PSi monolayer with porosity

61 % ($n_{PSi} = 1.83$ at $\lambda = 1.2$ μm), thickness (L) 2.1 μm, and pore size distribution varying from 50 to 250 nm was fabricated using a current density of 20 mA cm for 90 s (refractive index and porosity have been obtained by spectroscopic variable angle ellipsometry; data not shown here) [48]. The fresh-made PSi was placed in a Schlenk tube containing 3 mL of deoxygenated neat UDA (99 % v/v), 28 μL of $EtAlCl_2$ as a catalyst, and 100 μL of anhydrous toluene to improve its solubility in UDA. The reaction was conducted at 60 °C for 4 h in argon [32]. The hydrosilylated-PSi was extensively washed in THF and IPA.

2.6. *Spectroscopic reflectometry*

The optical setup to acquire the reflectivity spectra of PSi monolayer is made up of a white light source and the Ando AQ6315B optical spectra analyser (Yokohama Italia S.r.l, Nova Milanese, Italy), both connected to a Y reflection probe (Avantes, Apeldoorn, The Netherlands), through which the light is conveyed and subsequently collected to/from the sample at normal incidence. The optical spectra were performed from 800 to 1600 nm with a sampling wavelength of 1 nm. The reflectivity spectra are the result of the average of three independent measurements.

2.7. *Fluorescence microscopy*

Fluorescence images were acquired using a Leica AF6000LX-DM6M-Z microscope (Leica Microsystems, Mannheim, Germany), controlled by LAS-X (Leica Application Suite; rel. 3.0.13) software and equipped with a DFC7000T Leica camera. Fluorescence images were obtained using a 50 × objective and an I3 cube constituted by a 470 nm band-pass excitation filter.

2.8. *Covalent grafting of PNA-3 on PSi layer and cTnT recognition*

For the covalent grafting of PNA, the hydrosilylated PSi device was exposed to 100 μM of PNA-3 in the presence of EDC/NHS (0.040:0.016 mol L^{-1} in MES buffer, overnight, RT) and washed in deionized water [25].

For the sensing experiment, cTnT was solubilized in PBS 1 × (10 mmol L^{-1}, pH 7.4) at final concentrations of 0.02, 0.04, 0.08, and 0.16 ng mL^{-1}.

The biomolecular recognition was performed by incubating the Psi aptasensor with the cTnT solutions for 30 min at RT. After incubation, the sample was rinsed twice in deionized water and then dried by argon gas.

2.9. *Quantification of PNA-PSi surface functionalization*

The PNA-modified PSi chip was dissolved by incubating it with 100 μL of 2 mol L^{-1} NaOH for 30 min at RT. After incubation, the resulting solution was collected and analyzed by UV spectrophotometry at $\lambda_{max} =$ 258 nm to determine the concentration of PNA-3 released from the dissolved chip, using the Lambert-Beer law. Solutions of 2 mol L^{-1} NaOH and 1 μmol L^{-1} PNA-3 were used as the negative and the positive control, respectively [49,50].

3. Results and discussion

3.1. *Rational design of truncated PNA bioprobes for cTnT detection*

Conventional biorecognition elements, such as antibodies and DNA-based bioprobes, present several limitations when used in biosensor platforms. Antibodies, although highly specific, are prone to denaturation, require strict storage conditions, and exhibit variability between production batches. DNA-based bioprobes, while synthetically accessible and adaptable, are susceptible to nuclease degradation in biological fluids, limiting their stability and utility in real-world diagnostic applications [18].

To overcome these limitations, synthetic oligonucleotide analogs, such as peptide nucleic acids (PNAs), have garnered increasing attention. PNAs are DNA mimics in which the sugar-phosphate backbone is replaced by a pseudopeptide chain, imparting resistance to enzymatic degradation [25] and enhancing stability under thermal and chemical stress. Furthermore, due to the absence of electrostatic repulsion during duplex formation, PNAs exhibit stronger and more specific binding to complementary DNA or RNA strands [19,21].

PNAs can be engineered as aptamer-like probes for detecting proteins and small molecules, allowing them to form stable heteroduplexes with complementary nucleic acids or to be incorporated into more complex hybridization-based constructs. This structural and functional versatility makes PNAs highly suitable for a wide range of biosensing applications.[24] Despite these advantages, the relatively high cost of synthesizing PNAs, especially for longer sequences, poses a significant barrier to their widespread use in cost-sensitive diagnostic technologies.[25]

To address this challenge, a rational design strategy was employed to reduce the PNA sequence length while preserving binding capacity. Shorter sequences may also reduce steric hindrance and enhance target accessibility, which is advantageous for biosensor development [28].

A well-characterized 40-base DNA aptamer (WT) previously reported to exhibit high affinity for cardiac troponin T (cTnT) served as the starting point for sequence shortening [51,52]. Instead of directly translating the full-length sequence into a PNA analogue, truncation was pursued based on the hypothesis that shorter variants could retain sufficient binding affinity while reducing synthesis costs and improving chemical tractability [53].

The truncation process involved the progressive shortening of the wild-type PNA sequence while conserving key base pairs across the truncated variants (highlighted in yellow in Fig. 1), resulting in sequences ranging from 6 to 16 bases. Specifically, PNA-1 (6 bases), PNA-2 (8 bases), PNA-3 (12 bases), and PNA-4 (16 bases) were synthesized both with and without N-terminal acetylation to assess the effect on binding affinity. For all sequences, four Lys residues were added to the C-terminus of PNAs to enhance aqueous solubility and ensure functional stability under physiological conditions [54].

4. Molecular dynamics simulations

A combined computational approach, involving the use of molecular docking and molecular dynamics simulations (MDs), was employed to investigate the interaction sites of PNAs on the cTnT protein surface and to assess the dynamical stability of the resulting cTnT-PNA complexes. PNA ligands have been computationally investigated [55–57], also as potential partners of DNA and RNA strands [58–61], due to their structural advantages in the uncharged backbone. In this work, PNAs were simulated as single ligands capable of forming supramolecular structures with proteins. A previously used approach, based on the unbiased diffusion of one or more ligands to the surface of biological molecules [62–65], turned out to be very difficult to use, as it required extensive computational resources to capture the complex conformational landscape of the system efficiently. Therefore, following the pattern of work involving complexes between cTnT and aptamers [38, 66], the computational study was initiated from the complex structure obtained by docking and presenting the lowest score function. In this way, this starting configuration is realistic and suitable for molecular dynamics refinement. Each PNA sequence (PNA-1 to PNA-4, and PNA-WT) was relaxed along 400 ns of MDs, and the most representative structure obtained from the cluster analysis was then taken as a reference for subsequent docking on the cTnT (Fig. S12 and S13). The time evolution of the cTnT Root Mean Standard Deviation (RMSD) in Fig. S14 illustrates a highly flexible protein structure, both with and without PNA ligands. Without ligands, the initial 50 ns of each production replicate served as equilibration time, with the RMSD converging around 10–15 Å afterward. A and B helices exhibited an RMSD centered at 4–5 Å,

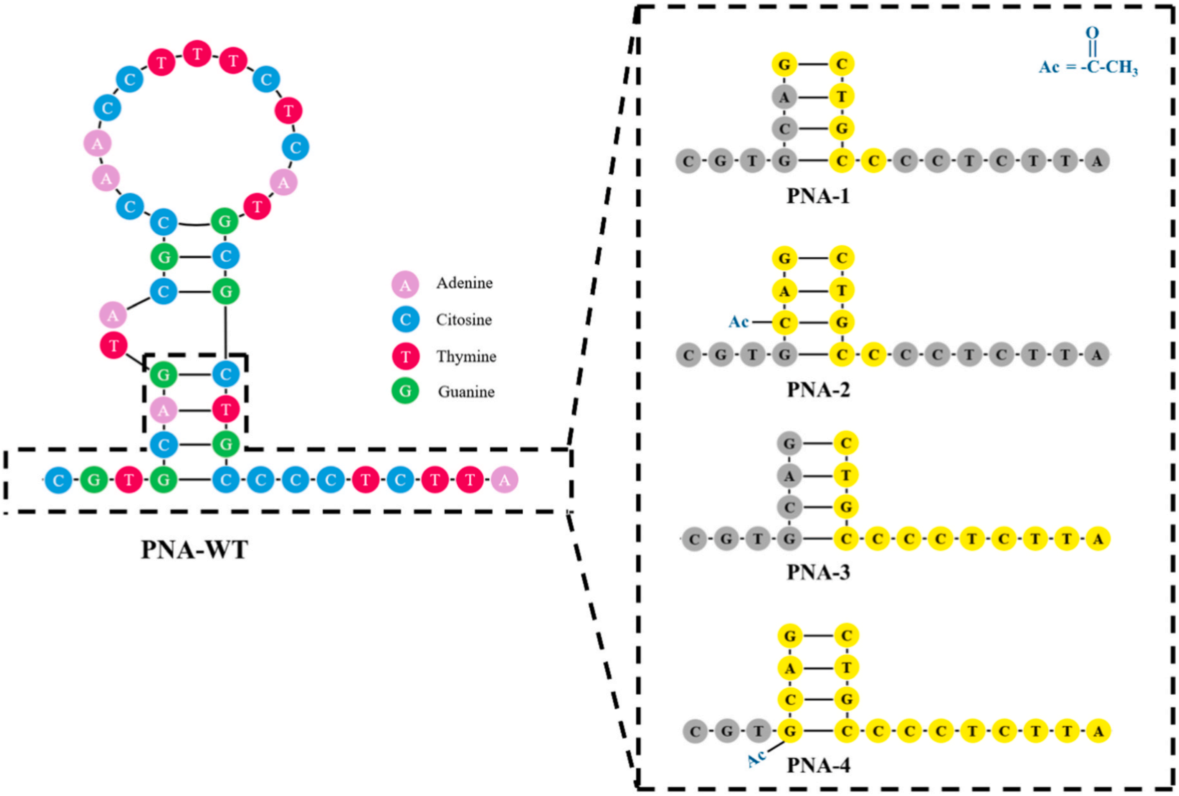

Fig. 1. Schematic representation of the 40-base starting PNA sequence (PNA-WT) and its corresponding truncated PNA variants (PNA-1 to PNA-4).

highlighting their inherent flexibility, as noted by the most visited clusters extracted during the dynamics, shown in Fig. S15. These structures highlighted protein conformations in which the two helices remain parallel or placed perpendicularly, rearranging contacts between them, and the overall folding is maintained. PNAs with the shortest sequences, PNA-1 and PNA-2, with 6 and 8 bases, respectively, tended to destabilize the protein structure, especially helix A, as evidenced by the RMSD (Fig. S14). Compared to the starting interaction site, the ligands slid mainly along helix B, allowing helix A to fold back on itself and change conformation (Fig. S15). The interaction was weaker, to the extent that the ligands were even able to fully detach themselves from the protein and move into the bulk solution (as indicated by the distance between the centers of mass of cTnT and the PNAs in Fig. S16). The presence of PNA-3 and PNA-4, containing 12 and 16 bases respectively, also allowed the protein to undergo structural rearrangement. Although the RMSD fluctuated significantly, the distributions indicated that the most probable values lay between those observed for cTnT alone and those complexed with PNA-1 or PNA-2. Moreover, complexation with PNA-3 stabilized helix A more than helix B. The most frequently sampled conformations showed that the helices tended to fold more extensively in the presence of PNA-4. Unlike PNA-1 and PNA-2, the ligands in this case rearranged around the initial binding site without detaching (Fig. S16).

Attention was also given to the PNA-WT sequence. The protein structure appeared to be more stabilized compared to the previously analyzed, also with reference to helix A (Fig. S14). The two helices were kept parallel, with the PNA acting as a bridge between them (Fig. S15). All PNAs were found to adopt a very compact conformation, as shown by the radius of gyration and its probability distributions (Fig. S17), and agglomeration state, dictated by strong interaction and π-stacking between the same bases. In the protein, as the above analyses had already shown, the turning radius was highly dependent on the presence of the ligand. Helix A retained its elongated conformation, especially with PNA-WT, while PNA-3 was the remaining ligand that caused the conformation to change the least. This is also emphasized by RMS fluctuations (RMSF), as shown in Fig. 2. The most flexible regions appeared to be the apical regions of the two helices, respectively, which tended to fold as described above. The general flexibility of the protein was strongly attenuated in the presence of PNA-WT. On the other hand, with PNA-3 and PNA-4, cTnT fluctuates more (Fig. S18). The computational analyses thus clarified how the length of the PNA strand can affect the stability of cTnT. The results suggest that a minimum sequence length is required to ensure stable binding of PNA to the protein. In this context, PNA-3 and PNA-4 appear particularly promising: despite being shorter and less complex than PNA-WT, they still effectively interact with cTnT, pointing to a more efficient and forward-looking approach.

4.1. *Assessment of PNA bioprobes recognition via Western blot analysis*

To support *in silico* predictions and validate the molecular recognition properties of the synthesized truncated PNA sequences, Western blot analysis was carried out as a qualitative tool [67]. Beyond its conventional application in protein detection, this technique allows the assessment of biomolecular interactions by monitoring shifts in protein electrophoretic mobility due to complex formation. This study provided critical experimental evidence of target engagement, allowing evaluation of binding specificity, concentration-dependent effects, and potential denaturation phenomena. cTnT was used as the target protein to determine whether its interaction with the PNAs led to detectable changes in its apparent molecular weight. This approach proved instrumental in identifying the PNA sequence with the best binding affinity, closely resembling that of the original WT sequence, and thus representing the most promising candidate for cost-effective biosensor development. A monoclonal anti-troponin antibody (anti human cTnT) was used in combination with SDS-PAGE to detect potential changes in the apparent molecular weight of cTnT upon interaction with PNAs. As illustrated in Fig. 3A, cTnT was resuspended in PBS 1 × at a concentration of 1 μg mL^{-1} before the addition of PNAs. After a 30-min

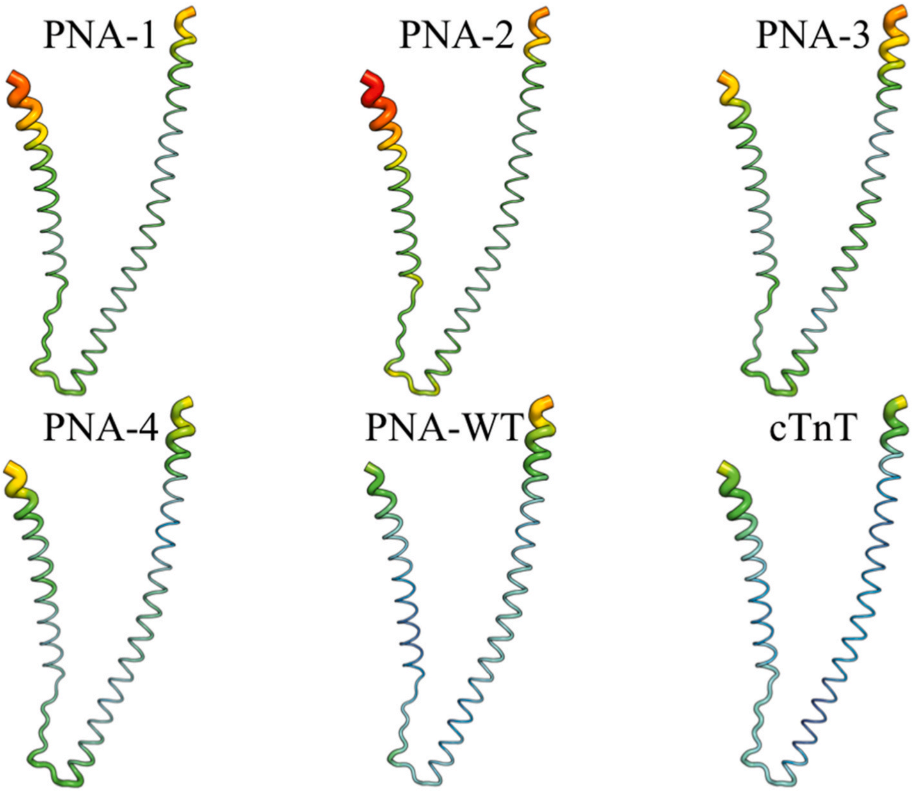

Fig. 2. 3D color maps of the cTnT RMS fluctuation (RMSF) in the presence (PNA-x) and absence (cTnT) of the PNA ligands. For each system, RMSF is shown by the color from blue (0 Å) to red (19 Å) and the thickness. (For interpretation of the references to color in this figure legend, the reader is referred to the Web version of this article.)

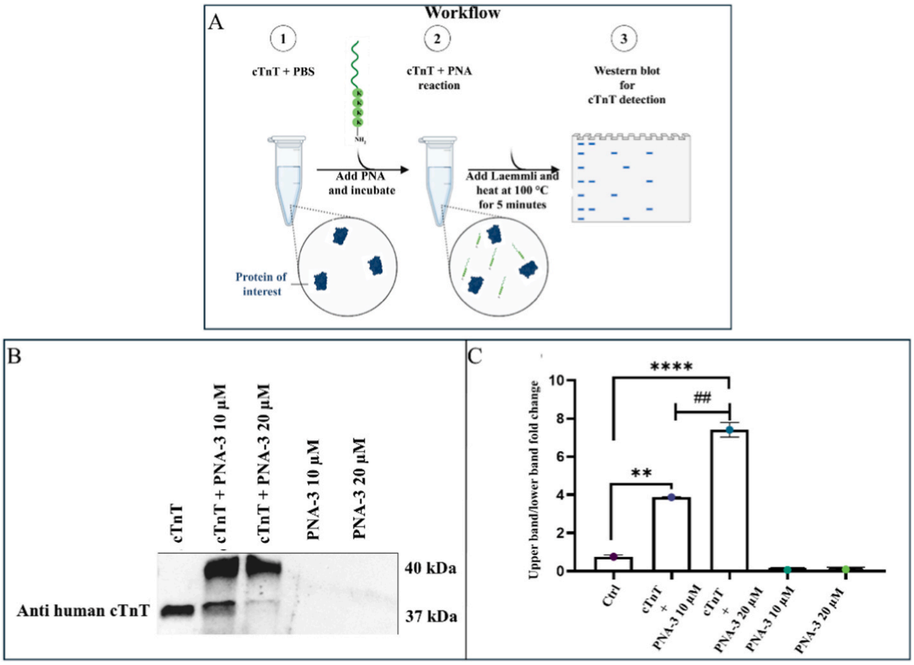

Fig. 3. (A) Schematic representation of the experimental workflow for cardiac troponin T (cTnT)-PNA-3 interaction by Western blot. The graphical scheme was produced by the authors using the BioRender platform (https://www.biorender.com/) (basic license terms). (B) Western blot analysis of cTnT alone (1 μg mL^{-1}), cTnT incubated with PNA-3 at two different concentrations, and PNA-3 control samples. Anti-human troponin mouse Ab was used to detect cTnT on the gel. Each experiment was performed in three technical replicates. (C) Fold change of cTnT derived from protein quantification of morphodensitometric analysis of upper and lower bands performed by ImageJ. Data are expressed as the mean ± SD. Unpaired Student's t-test with $^{**}p < 0.01$; $^{****}p < 0.0001$ vs ctrl and $^{\#\#}p < 0.01$ vs cTnT + PNA-3 20 μM sample.

incubation, the Western blot protocol was carried out as detailed in the Materials and Methods section. Western blot results revealed that the cTnT protein forms the most stable protein/PNA complex when incubated with PNA-3 (Fig. S19). A band corresponding to cTnT alone, serving as a positive control, was observed at 37 kDa. This band accounts for approximately 85 % of the cTnT fragments typically detected in blood following an acute myocardial infarction [68]. Notably, an additional band of higher molecular weight was observed in the sample containing both cTnT and PNA-3, suggesting the formation of a complex between cTnT and PNA-3. As shown in Fig. 3B, increasing the concentration of PNA-3 from 10 to 20 μmol L^{-1} led to a decrease in the intensity of the lower band corresponding to the unbound cTnT. As expected, PNA-3 alone, included as a negative control, did not produce any detectable signal for cTnT.

More in detail, as shown in Fig. 3C, a statistically significant increase in the apparent molecular weight of cTnT was observed upon binding with PNA-3 at 10 μmol L^{-1} compared to the control ($p < 0.01$). The effect was more pronounced at 20 μmol L^{-1}, with a significant shift compared to both the control ($p < 0.0001$) and the 10 μmol L^{-1} condition ($p < 0.01$). The concentration-dependent effects observed indicate that higher concentrations of PNA-3 lead to more pronounced binding interactions, which could be pivotal for enhancing sensitivity in diagnostic applications related to MI.

A scrambled PNA sequence (ctrl PNA) was tested to assess binding specificity and did not produce any higher molecular weight bands, indicating no complex formation (Fig. S20). In addition, PNA-3 was tested against macrophage migration inhibitory factor (MIF), a peripheral blood protein that is upregulated in response to myocardial ischemia [69], and no upper molecular weight band was observed, further corroborating the specificity of PNA-3 for cTnT (Fig. S20).

4.2. Fabrication of porous silicon optical transducer and surface functionalization

The optical transducer used for the development of the label-free biosensor was obtained through electrochemical etching of crystalline silicon wafers, a well-established low-cost technique that enables precise tuning of both the morphological and optical properties of the resulting PSi structures. This method, based on the anodic dissolution of silicon in HF-containing electrolytes under controlled current densities, allows for the fabrication of highly ordered porous matrices with defined pore size, porosity, and thickness. In this case, the process parameters were optimized to generate a macroporous monolayer (pores size >50 nm), characterized by a large surface area and suitable optical transducer properties [70]. This structure demonstrated its ability to maximize probe immobilization (up to 15–20 DNA- or PNA-based bioprobes) while maintaining high accessibility for target molecules, thereby enhancing the sensitivity and selectivity of the biosensor [25,71]. The as-etched PSi transducer was subsequently functionalized through a series of chemical modifications, as schematically illustrated in Fig. 4, to obtain the final biosensor configuration.

The freshly etched PSi surfaces are terminated with reactive Si–Hx species, which make the material susceptible to oxidation and degradation in aqueous environments. This instability not only compromises the structural integrity of the porous matrix but also affects the reliability of its optical response over time, a critical factor for label-free sensing applications. To address this issue, a surface passivation strategy was carried out based on a recently developed hydrosilylation method using UDA, which combines mild temperature (60 °C) and $EtAlCl_2$. This approach significantly reduced reaction times and eliminated the need for the high-temperature conditions typically required in conventional protocols (Fig. 4, I) [32]. This surface modification not only passivates the surface by replacing unstable Si–Hx bonds with more robust Si–C bonds but also introduces COOH functional groups, which serve as anchoring sites for the subsequent covalent immobilization of selected truncated PNA probe (PNA-3) [25].

In this study, spectroscopic reflectometry was used as a key analytical label-free technique to monitor the optical response of the PSi transducer throughout the surface modification process. The interaction of inorganic or organic species with the pore walls alters the average refractive index of the porous layer, resulting in measurable shifts in the reflectivity spectrum. Due to the intrinsic interferometric properties of

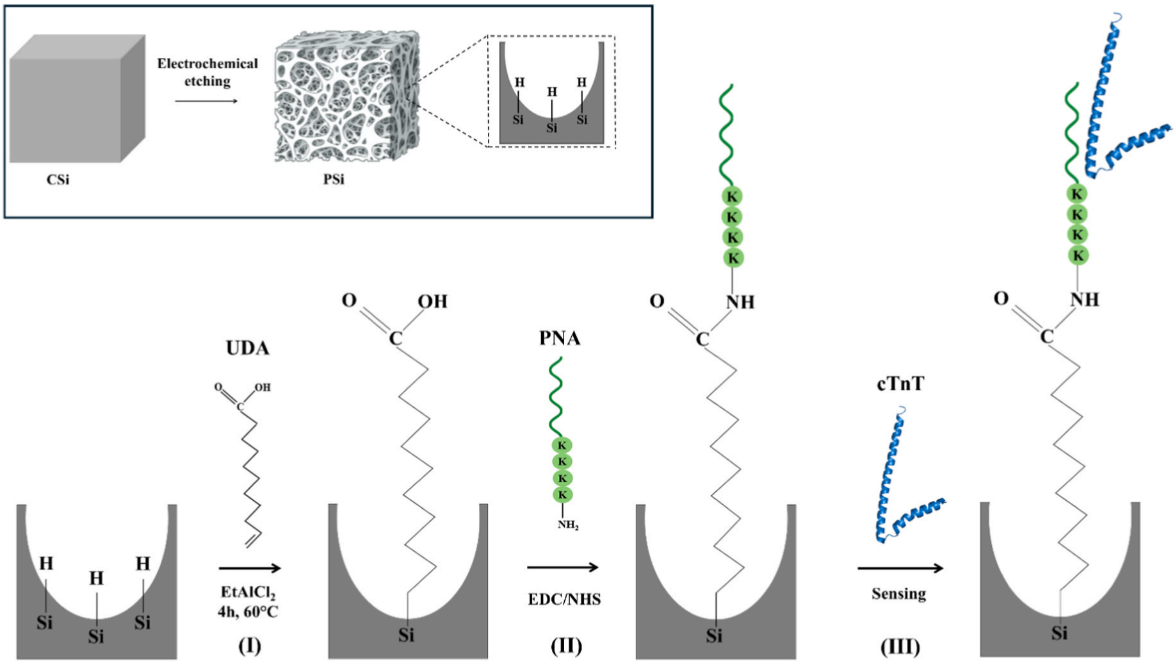

Fig. 4. Schematic representation of the chemical strategy for the development of PNA-based macroporous silicon (PSi) label-free optical biosensor for cardiac troponin T (cTnT) detection. (I) Surface functionalization of the as-etched PSi via mild hydrosilylation condition with undecenoic acid (UDA) (4 h at 60 °C, in the presence of $EtAlCl_2$); (II) Covalent immobilization of the truncated PNA-3 probe using EDC/NHS coupling chemistry; (III) Detection of cTnT by exposing the obtained PSi biosensor to increasing target concentrations.

PSi, the layer behaves as a Fabry–Pérot cavity, where material infiltration into the pores modifies the optical path length [72]. The Fast Fourier Transform (FFT) analysis of the reflectivity spectra provides a straightforward and reliable approach to monitor variations in the average refractive index of the PSi layer. In this analysis, the optical thickness (OT), defined as the product of the PSi effective refractive index (n_{psi}) and its physical thickness (L), was determined from the position of the main peak in the FFT spectrum, which corresponds to twice the optical thickness (2 OT) of the layer [25]. Changes in OT (nPSi × L) were therefore used as a quantitative indicator of molecular adsorption or binding events occurring within the porous matrix.

Reflectivity spectra acquired at normal incidence before and after hydrosilylation (PSi-UDA) are shown in Fig. 5A, along with the corresponding FFT profiles in Fig. 5B. As the physical thickness (L) of the porous layer was fixed at 2100 nm, the observed red-shift of approximately 25 ± 5 nm in the reflectivity spectrum translated into a 200 ± 40 nm shift in the FFT peak position. This spectral shift reflects an increase in the average refractive index of the PSi layer, clearly indicating the formation of an organic layer on the pore walls because of the hydrosilylation process [25].

The successful introduction of carboxyl functional groups on the PSi surface was further confirmed by fluorescence microscopy (Fig. 5C). To evaluate both their presence and accessibility, carbodiimide chemistry was employed to covalently immobilize a model fluorescent bioprobe (PrA* 100 μmol L^{-1}) containing a primary amine group. The resulting fluorescence signal, normalized to the device area, exhibited a 1.35-fold increase in the hydrosilylated PSi (PSi–UDA–PrA*) compared to the unmodified crystalline silicon (CSi) as control. These findings indirectly confirm the presence of reactive carboxyl groups capable of forming stable bonds with amine-functionalized biomolecules, as further supported by reflectivity spectra recorded before and after PrA* conjugation (Fig. S21).

The stability of the PSi-UDA surface was thoroughly evaluated by exposing the sample to stability tests in PBS 1 × (pH 7.2) for 2 h, a condition selected due to its relevance to aqueous functionalization protocols and commonly used in sensing applications. No shifts or variations were observed in the reflectivity spectra, as shown in Fig. 5D and E. This is particularly important, as previously demonstrated that not properly stabilized PSi structures undergo rapid degradation (within minutes) in aqueous environments [70]. The absence of significant spectral changes confirms the stability of the functionalized PSi surface under the tested conditions, supporting its suitability for subsequent biosensor development.

4.3. Stepwise chemical strategies for the development of a PNA-based PSi label-free biosensor

To optimize the analytical performance of PSi-based biosensors, several strategies have been explored to refine the surface architecture and molecular arrangement within the porous matrix. Among these, increasing pore size to accommodate recognition elements and adjusting probe concentration to modulate surface density have shown promising results [73]. However, these approaches are not without limitations. Excessive pore enlargement can compromise the optical quality of the PSi transducer, reducing the resolution and sensitivity of interferometric detection. Similarly, increasing the concentration of bioprobes, while potentially enhancing target binding, can result in steric hindrance and uneven distribution within the pores, ultimately affecting both target

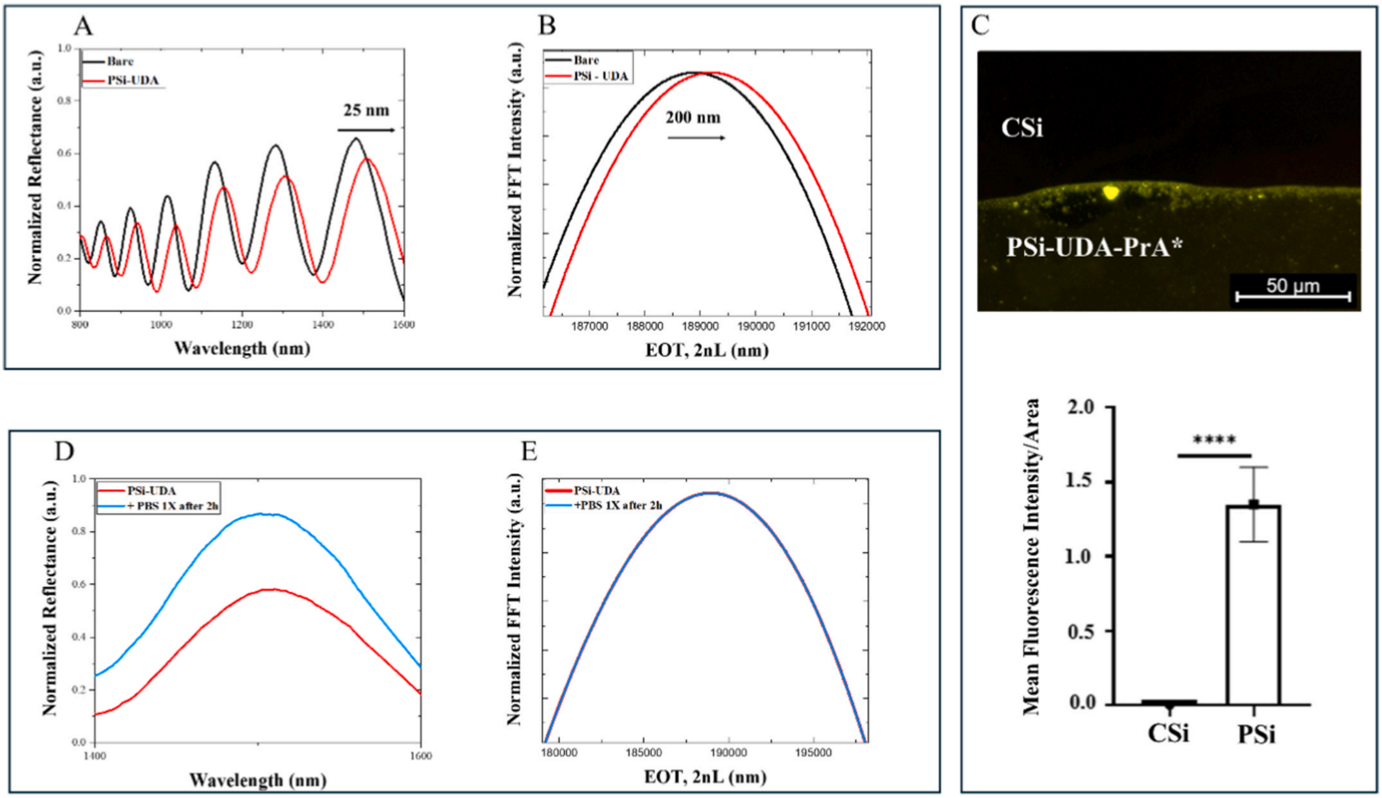

Fig. 5. (A) Reflectivity spectra and (B) corresponding Fourier transforms of the PSi biosensor before (black line) and after the mild hydrosilylation process (red line). Data represent the mean of three independent measurements. (C) Fluorescence microscopy image of the hydrosilylated PSi chip (PSi-UDA) after incubation with Protein A-FITC (PSi-UDA-PrA*), along with the quantitative analysis of the mean fluorescence intensity normalized to area. The ratio between the crystalline silicon (CSi) region and the PSi-UDA-PrA* region is shown. Data are presented as mean fluorescence intensity/area ±SD. Statistical significance: ****$p < 0.0001$ versus CSi ($n \geq 3$). (D) Reflectivity spectra and (E) corresponding Fourier transforms of the PSi-UDA device before (red line) and after stability testing in 1 × PBS for 2 h (light blue line).

accessibility and signal reproducibility.

In this context, the use of shorter bioprobes represents a valuable strategy for the development of high-performance, cost-effective biosensors. These probes not only reduce synthesis cost, but also enable improved control over surface density, minimizing steric hindrance and promoting a more uniform and functional arrangement within the porous matrix.

To achieve covalent immobilization of the selected PNA probe (PNA-3) onto the PSi surface for the development of a label-free PSi biosensor (Fig. 4, II), three different experimental conditions were tested to exclude nonspecific adsorption and to identify the optimal pH for the carbodiimide-mediated coupling. Given the pH dependence of carbodiimide chemistry, conjugation was tested at pH 5.5 and pH 7.0, both commonly reported in the literature to support EDC/NHS activation [25,74]. The highest immobilization efficiency was observed at pH 5.5 (Fig. 6C), as indicated by a 40 ± 8 nm red shift in the reflectivity spectrum and a 200 ± 40 nm shift in the FFT peak (Fig. 6F), reflecting a significant increase in the effective refractive index due to probe binding. At pH 7.0 (Fig. 6B), a 16 ± 2 nm reflectivity shift and a 100 ± 12 nm FFT shift were recorded (Fig. 6E), indicating lower coupling efficiency. In contrast, the absence of EDC/NHS activation (Fig. 6A) resulted in only a minor shift of 5 ± 1 nm in reflectivity and 37 ± 7 nm in FFT (Fig. 6D), confirming limited nonspecific adsorption.

The sample functionalized at pH 5.5 was selected for subsequent sensing applications. To confirm the stability of the covalently immobilized bioprobe under aqueous conditions, the PNA-functionalized device was incubated in PBS 1 × (pH 7.2) for 2 h. As shown in Fig. S22, no appreciable shift in the reflectivity spectra was detected after incubation, confirming strong and stable attachment of the PNA to the PSi matrix, ensuring reliability during sensing operations.

This test was aimed exclusively at assessing the chemical and optical stability of the PNA–PSi interface under controlled buffer conditions, demonstrating the robustness of the covalent immobilization strategy.

To quantify the degree of surface functionalization, the amount of immobilized PNA (PNA-3) on the PSi surface was measured. The conjugated PNA was released by incubating the PSi chip in NaOH for 30 min, a treatment that selectively dissolved the PSi matrix while preserving the underlying CSi (Fig. S23) [75,76]. The concentration of detached PNA was determined spectroscopically using the Lambert–Beer law. Based on an initial PSi mass of 0.2 mg, the amount of immobilized PNA was calculated to be 1.7 ± 0.4 × 10^{-6} mol g^{-1}. To express the functionalization in surface density units (mol cm^{-2}), the specific surface area (SSA) of the PSi was used. According to previous work on a similar PSi-based aptasensor, the SSA was determined to be 153 m^2 g^{-1} using Brunauer–Emmett–Teller (BET) analysis and a simplified cylindrical pore model [71]. Using this value, the surface coverage was estimated to be 1.12 ± 0.30 pmol cm^{-2}, calculated as the ratio between the immobilized PNA and the PSi surface area.

4.4. *Performance testing of the PNA biosensor: target recognition, sensitivity, and limits of detection*

The troponin complex, composed of three subunits (troponin I, T, and C) regulates calcium-mediated contraction in striated muscle [4,11,14]. Among these, cTnI and cTnT are the most specific and sensitive biomarkers for diagnosing MI, due to their exclusive expression in cardiac muscle and their direct correlation with myocardial injury. In contrast, cTnC lacks cardiac specificity because its isoform is also present in slow-twitch skeletal muscle, making it less suitable as a cardiac biomarker [4,14].

In this context, cTnT has gained particular attention in clinical diagnostics. In healthy individuals, its serum concentration remains

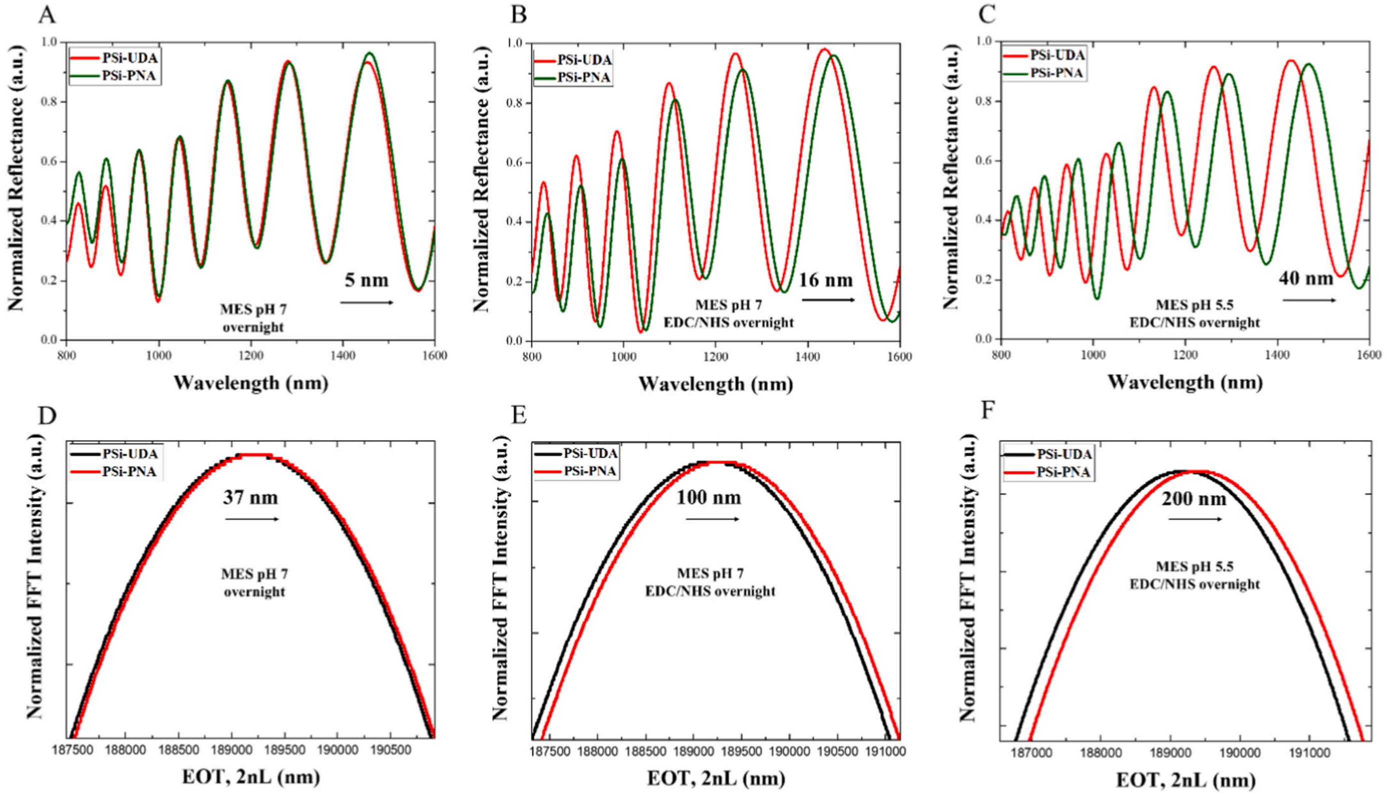

Fig. 6. Reflectivity spectra of the hydrosilylated device (PSi-UDA) before and after overnight incubation with the selected PNA (PNA-3) under three different conditions: (A) incubation in MES buffer (pH 7) without activation; (B) incubation in MES buffer (pH 7) with EDC/NHS activation; (C) incubation in MES buffer (pH 5.5) with EDC/NHS activation. The corresponding Fourier transforms are shown in (D), (E), and (F), respectively. All data are expressed as the mean of three independent measurements.

extremely low (typically <0.01 ng mL^{-1}), whereas in pathological conditions such as MI, levels can rise sharply, often exceeding 10 ng mL^{-1} and reaching over 100 ng mL^{-1} in severe cases [77]. Thus, achieving reliable quantification within the sub-nanogram-per-milliliter range is particularly relevant for early diagnosis and rapid clinical decision-making, consistent with the aim of this proof-of-concept study to demonstrate a highly sensitive platform for early cTnT detection.

To evaluate the target recognition performance of the developed label-free biosensor, the PNA-based PSi device was exposed to increasing concentrations of cTnT (0.02, 0.04, 0.08, and 0.16 ng mL^{-1}) (Fig. 4, III). The binding events between the immobilized PNA probe and the target analyte were monitored by analyzing the changes in the reflectivity spectra of the device, which exhibited clear red shifts correlated with the cTnT concentration (Fig. 7A). In this configuration, the PNA–cTnT complex forms a highly stable covalent assembly that cannot be dissociated under mild regeneration conditions [71]. The biosensor is therefore intended for single use, a choice consistent with point-of-care applications where disposable formats ensure reliability and prevent cross-contamination.

The dose-dependent optical response was further validated by a calibration curve of ΔEOT as a function of cTnT concentration, yielding a strong linear correlation ($R^2 = 0.98$) (Fig. 7B). Within the linear response range, the biosensor demonstrated a sensitivity of 576 ± 48 nm ng^{-1} mL. Based on the calibration curve and the corresponding sensitivity, the limit of detection (LoD) was determined. The LoD defines the lowest analyte concentration that produces a measurable optical signal distinguishable from the background noise, thus representing the minimum detectable concentration for the developed PSi-based optical platform. A calculated LoD of $0.030 \pm 2.0 \times 10^{-5}$ ng mL^{-1} was obtained according to the 3σ/S criterion, where σ represents the standard deviation of the blank signal and S the slope of the calibration curve [72]. As part of the performance testing, a negative control was included, using PSi-UDA exposed to the maximum concentration of cTnT (0.16 ng mL^{-1}). No significant red shift was observed, indicating the absence of non-specific binding or recognition (Fig. S24), confirming the specificity of the PNA biosensor. In addition, during the analytical tests the device was sequentially exposed for approximately 30 min to each of the four tested analyte concentrations, without any detectable degradation or baseline drift, further demonstrating the robustness of the PNA–PSi interface under repeated use within the same assay. These results furthetr confirm that the newly designed truncated PNA probes can form a stable and durable linkage with the PSi surface, providing a solid foundation for subsequent investigations in more complex biological environments.

These results are particularly significant, as the developed biosensor achieved a LoD in the picogram-per-milliliter range, outperforming previous PSi-based devices that employed longer DNA or PNA probes, which typically exhibit LoD in the nanomolar range [25,48]. This improved performance is probably attributable to more efficient and uniform surface functionalization enabled by the use of a shorter PNA probe, which minimizes steric hindrance and optimizes probe orientation within the porous matrix.

While examples in the literature report lower LoDs (e.g., 6.0 ± 1.0 pg mL^{-1}) for cTnT detection using longer PNA sequences in combination with more advanced nanostructured transducers [24], the performance achieved in this work remains within the same order of magnitude, despite employing a simpler and more cost-effective platform (Table 2). These findings highlight the critical importance of molecular probe design and suggest that combining short, highly specific bioreceptors with more sensitive optical supports could further reduce detection limits, potentially reaching the femtomolar range, while maintaining low-cost fabrication.

5. Conclusions

In this study, a label-free biosensor based on a porous silicon (PSi) transducer was developed and optimized for the detection of cardiac troponin T (cTnT), a highly specific and clinically relevant biomarker for early diagnosis of myocardial infarction (MI). A truncation strategy was applied to a previously validated 40-mer sequence, resulting in a set of shorter PNA probes. Among them, a 12-mer (PNA-3) was identified as the most effective, based on both computational prediction and experimental validation through Western blot analysis.

PSi surface passivation and functionalization were achieved through mild hydrosilylation and monitored by reflectance spectroscopy at each step, confirming the successful introduction of carboxylic groups and subsequent covalent immobilization of the PNA via EDC/NHS coupling. Conjugation was optimized at pH 5.5, resulting in an efficient functionalization with a surface density of 1.12 ± 0.30 pmol cm^{-2}. The modified surface exhibited strong stability in aqueous conditions, confirming its suitability for real-time sensing applications.

The biosensor demonstrated specific, concentration-dependent

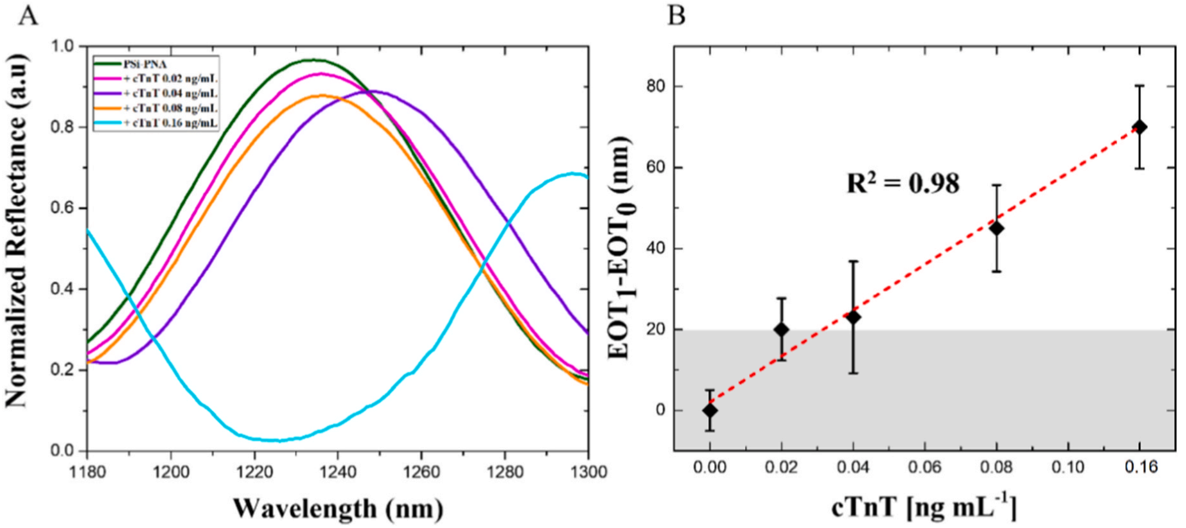

Fig. 7. (A) Reflectivity spectra of the PNA based PSi biosensor (PSi-PNA) after exposure to increasing concentrations of cTnT (0.02, 0.04, 0.08, and 0.16 ng mL^{-1}). (B) Calibration curve of ΔEOT (Effective Optical Thickness shift) as a function of cTnT concentration. A linear fit (red line) was applied to the low-concentration range to determine the sensitivity and limit of detection (LoD) of the sensor. The R^2 value represents the coefficient of determination, indicating the proportion of variance in ΔEOT explained by cTnT concentration. Error bars indicate the standard deviation (SD) from three independent measurements (n = 3).

Table 2
Comparison of representative optical and electrochemical biosensors for cardiac troponin T.

Assay	LoD (ng mL^{-1})	Linear range (ng mL^{-1})	Assay time	Sample matrix	Transducer/Type	Label/Label-free	Reference
Integrated nanoslit array fluidic diode sensor	1×10^{-5} (buffer); 1×10^{-2} (serum)	1–100	<10 min	PBS buffer, human serum	Nanofluidic diode (current-based)	Label-free	Liu, Y.; et al.; *Nano Lett.* 2014, 14(12), 6983–6990.
Portable nanoporous electrical biosensor	1×10^{-5}	1×10^{-6}–10	Rapid (<10 min)	7 % BSA (model serum buffer)	Impedance on nanoporous membrane	Label-free	Shanmugam, N. R.; et al. *Future Sci. OA* 2015, 1(3), FSO24.
Aptasensor on gold (SAM)	0.01	0.05–5	~1 h	PBS buffer	Electrochemical aptasensor (Au)	Labeled (ferro/ferricyanide redox)	Negahdary M.; et al., *Int. J. Mol. Cell. Med.* 2019, 8(4), 271.
Fluorescence FRET immunosensor	0.12	0.1–50	Rapid (<10 min)	Buffer, human serum	Fluorescence (FRET, carbon dot/MoS$_2$)	Labeled (antibody-based)	Gogoi, S; et al., *Phys. Chem. Chem. Phys.* 2018, 20(24), 16501–16509.
ZnO EIS nanostructured biosensor	1×10^{-4}	0.05–25 ng mL^{-1}	Rapid (<10 min)	Human serum	Electrochemical impedance (ZnO nanostructure)	Label-free	Shanmugam, N. R.; et al. *Nanomedicine* 11.11 (2016): 1345–1358.
This work (short-PNA/PSi, proof-of-concept)	0.03	0.02–0.16	~30 min	PBS buffer	Porous silicon optical interferometer	Label-free	This study

detection of cTnT across a clinically relevant range (0.02–0.16 ng mL^{-1}), with negligible non-specific adsorption. A limit of detection of 0.030 ± 2.0×10^{-5} ng mL^{-1}was achieved, placing the device performance within the same order of magnitude as more complex and costly sensing platforms. This proof-of-concept study demonstrates the feasibility of integrating short, rationally designed PNA probes onto a low-cost PSi optical transducer, establishing a stable and reliable biosensing interface for cTnT detection.

Analytical validation under controlled buffer conditions confirmed the robustness of the surface chemistry and the reproducibility of the PNA–PSi platform, consolidating its potential as a cost-effective analytical system.

As a proof-of-concept, the present work focuses exclusively on the analytical phase, providing the fundamental basis for future testing in biologically relevant matrices. Planned developments include spike-and-recovery assays in serum and plasma, interference studies, and cross-reactivity evaluations to assess diagnostic feasibility.

This approach can be further expanded toward a multiplexed proof-of-concept biosensor for the simultaneous detection of multiple cardiovascular biomarkers (PD-L1, BNP, MMP-9, hs-CRP) [78,79].

The combination of short, sequence-specific PNA probes with low-cost PSi technology paves the way for affordable, high-performance point-of-care diagnostics, enabling earlier and more accessible cardiovascular assessment.

CRediT authorship contribution statement

Maria Grazia Nolli: Writing – original draft, Methodology, Investigation, Formal analysis, Data curation. **Alessio Bartocci:** Methodology, Formal analysis, Data curation. **Caterina De Rosa:** Methodology, Formal analysis, Data curation. **Andrea Patrizia Falanga:** Methodology. **Vincenzo Abbate:** Methodology, Data curation. **Monica Terracciano:** Writing – review & editing, Writing – original draft, Methodology, Investigation, Funding acquisition, Formal analysis, Data curation. **Valeria Nocerino:** Methodology. **Ilaria Rea:** Data curation, Conceptualization. **Luca De Stefano:** Conceptualization. **Sabrina Giordano:** Methodology. **Gennaro Piccialli:** Funding acquisition. **Marco Fabio Costantino:** Methodology. **Carminia Maria Della Corte:** Methodology. **Elise Dumont:** Methodology. **Nicola Borbone:** Writing – review & editing, Investigation, Funding acquisition, Formal analysis, Conceptualization. **Giovanni Orabona Dell'Aversana:** Conceptualization. **Giorgia Oliviero:** Writing – original draft, Supervision, Resources, Investigation, Funding acquisition, Data curation, Conceptualization.

Declaration of competing interest

The authors declare no conflict of interest.

Acknowledgments

The authors acknowledge financial support from the Finanziamento della Ricerca di Ateneo 2022"MULTIPARAMETRIC HYBRID APTASENSOR FOR CARDIOVASCULAR DISEASE EARLY DIAGNOSIS" (ID: FRA_2022_MultiHybridA), Universy of Naples Federico II. The authors acknowledge financial support from European Union NextGenerationEU [IR0000010 "ELIXIRxNextGenIT", PNRR MUR-M4C2—Investment 3.1, CUP UNINA: B53C22001800006; P2022YJZ5F "Small Molecule Anticancer Ligands Library from mediterranean plants (SMALL)", PNRR 2022 MUR-M4C2—Investment 1.1, CUP UNINA: B53D23025910001; P2022KY45H "Anticancer Phodynamic Treatment using Aptamers for Medical Enhanced Resective Surgery (APTAMERS)", PNRR 2022 MUR-M4C2–Investment 1.1, CUP UNINA: E53D23020510001] and CN00000041 "National Center for Gene Therapy and Drugs based on RNA Technology", National Recovery and Resilience Plan (NRRP), Mission 4 Component 2 Investment 1.4, CUP E63C22000940007].

The authors thank Dr. Luca Ricciardi of the Mass Spectrometry Laboratory, Department of Pharmacy, University of Naples Federico II, for mass spectrometry analysis, and Dr. Valentina Roviello of the University Service Center for Life Sciences and Technologies (CESTEV), University of Naples Federico II, for her contribution to the laboratory work involved in this study.

Appendix A. Supplementary data

Supplementary data to this article can be found online at https://doi.org/10.1016/j.talanta.2025.129054.

Data availability

Data is contained within the article and supplementary material. The data that support the findings of this study are available from the corresponding author upon reasonable request.

References

[1] N. Salari, F. Morddarvanjoghi, A. Abdolmaleki, S. Rasoulpoor, A.A. Khaleghi, L. A. Hezarkhani, S. Shohaimi, M. Mohammadi, The global prevalence of myocardial infarction: a systematic review and meta-analysis, BMC Cardiovasc. Disord. 23 (1) (2023) 206, https://doi.org/10.1186/s12872-023-03231-w.

[2] Y. Gerber, S.A. Weston, M. Enriquez-Sarano, C. Berardi, A.M. Chamberlain, S. M. Manemann, R. Jiang, S.M. Dunlay, V.L. Roger, Mortality associated with heart

failure after myocardial infarction: a contemporary community perspective, Circ Heart Fail 9 (1) (2016) e002460, https://doi.org/10.1161/CIRCHEARTFAILURE.115.002460.

[3] P. Peng, C. Liu, Z. Li, Z. Xue, P. Mao, J. Hu, F. Xu, C. Yao, M. You, Emerging ELISA derived technologies for in vitro diagnostics, TrAC, Trends Anal. Chem. 152 (2022) 116605, https://doi.org/10.1016/j.trac.2022.116605.

[4] S. Ebrahimi, V. Alivirdiloo, M. Hajiabbasi, S. Masoumi, M. Mohammadi, S. Hosseini, S.O. Gargari, A. Mobed, Cardiac troponin I biosensors: innovations in real-time diagnosis of cardiovascular diseases, Anal Sci Adv 6 (1) (2025) e70009, https://doi.org/10.1002/ansa.70009.

[5] I.H. Elrobaa, K. Khan, E. Mohamed, The role of Point-of-Care testing to improve acute care and health care services, Cureus 16 (3) (2024) e55315, https://doi.org/10.7759/cureus.55315.

[6] M.H. Shafie, M. Antony Dass, H.S. Ahmad Shaberi, Z. Zafarina, Screening and confirmation tests for SARS-CoV-2: benefits and drawbacks, Beni Suef Univ J Basic Appl Sci 12 (1) (2023) 6, https://doi.org/10.1186/s43088-023-00342-3.

[7] E. Sheikhzadeh, S. Eissa, A. Ismail, M. Zourob, Diagnostic techniques for COVID-19 and new developments, Talanta 220 (2020) 121392, https://doi.org/10.1016/j.talanta.2020.121392.

[8] Z. Tavakoli, F. Ranjbar, S.H. Tackallou, B. Ranjbar, Nanostructures for the prevention, diagnosis, and treatment of COVID-19: a review, Part Part Syst Charact 42 (1) (2025) 2400083, https://doi.org/10.1002/ppsc.202400083.

[9] P. Fitzgerald, S.W. Goodacre, E. Cross, S. Dixon, Cost-effectiveness of point-of-care biomarker assessment for suspected myocardial infarction: the randomized assessment of treatment using panel assay of cardiac markers (RATPAC) trial, Acad. Emerg. Med. 18 (5) (2011) 488–495, https://doi.org/10.1111/j.1553-2712.2011.01068.x.

[10] A. Campu, I. Muresan, A.-M. Craciun, S. Cainap, S. Astilean, M. Focsan, Cardiac troponin biosensor designs: current developments and remaining challenges, Int. J. Mol. Sci. 23 (14) (2022) 7728, https://doi.org/10.3390/ijms23147728.

[11] Y. Qi, M. Cai, Y. Kang, J. Liu, Progress in biomarkers and diagnostic approaches for myocardial infarction, Clin. Chim. Acta 579 (2025) 120629, https://doi.org/10.1016/j.cca.2025.120629.

[12] K.A. Krychtiuk, L.K. Newby, High-sensitivity Cardiac troponin assays: ready for prime time, Annu. Rev. Med. 75 (2024) 459–474, https://doi.org/10.1146/annurev-med-051022-113931.

[13] J.H. Kristensen, D. Westermann, B. Lindahl, E. Giannitsis, A.S. Jaffe, Half-life and clearance of cardiac Troponin I and Troponin T in humans, Circulation 150 (2024) 1187–1198, https://doi.org/10.1161/CIRCULATIONAHA.123.066565.

[14] J. Mair, The pathophysiology of cardiac Troponin release and the various circulating cardiac Troponin Forms—Potential clinical implications, J. Clin. Med. 14 (2025) 4241, https://doi.org/10.3390/jcm14124241.

[15] A. Clerico, M. Zaninotto, A. Aimo, A. Padoan, C. Passino, A. Fortunato, C. Galli, M. Plebani, Advancements and challenges in high-sensitivity cardiac troponin assays: diagnostic, pathophysiological, and clinical perspectives, Clin. Chem. Lab. Med. 63 (2025) 1260–1278, https://doi.org/10.1515/cclm-2024.

[16] O. Ola, A. Akula, L. De Michieli, M. Dworak, E. Crockford, R. Lobo, N. Rastas, J. D. Knott, R.A. Mehta, D.O. Hodge, E. Grube, S. Karturi, S. Wohlrab, T. Tak, C. Cagin, R. Gulati, A.S. Jaffe, Y. Sandoval, Clinical impact of high-sensitivity cardiac troponin T implementation in the community, J. Am. Coll. Cardiol. 77 (25) (2021) 3160–3170, https://doi.org/10.1016/j.jacc.2021.04.050.

[17] L. Koechlin, J. Boeddinghaus, D. Doudesis, P. Lopez-Ayala, T. Zimmermann, K. Rumora, et al., Diagnostic and prognostic performance of high-sensitivity cardiac troponin T vs I, J. Am. Coll. Cardiol. 85 (4) (2025) 381–385, https://doi.org/10.1016/j.jacc.2024.10.076.

[18] D.X. Wang, J. Wang, Y.X. Wang, Y.C. Du, Y. Huang, A.N. Tang, Y.X. Cui, D. M. Kong, DNA nanostructure-based nucleic acid probes: construction and biological applications, Chem. Sci. 12 (22) (2021) 7602–7622, https://doi.org/10.1039/d1sc00587a.

[19] T. Crisci, A.P. Falanga, M. Casalino, N. Borbone, M. Terracciano, G. Chianese, M. Gioffrè, S. D'errico, M. Marzano, I. Rea, L. De Stefano, G. Oliviero, Bioconjugation of a PNA probe to zinc oxide nanowires for label-free sensing, Nanomaterials 11 (2) (2021) 1–17, https://doi.org/10.3390/nano11020523.

[20] K.P. Nandhini, D. Al Shaer, F. Albericio, B.G. de la Torre, The challenge of peptide nucleic acid synthesis, Chem. Soc. Rev. 52 (8) (2023) 2764–2789, https://doi.org/10.1039/d2cs00049k.

[21] A.P. Falanga, F. Greco, M. Terracciano, S. D'Errico, M. Marzano, S. Feola, V. Sepe, F. Fontana, I. Piccialli, V. Cerullo, H.A. Santos, N. Borbone, Engineering an oncolytic adenoviral platform for precise delivery of antisense peptide nucleic acid to modulate PD-L1 overexpression in cancer cells, Int J Pharm 668 (2025) 124941, https://doi.org/10.1016/j.ijpharm.2024.124941.

[22] Q. Lai, W. Chen, Y. Zhang, Z. Liu, Application strategies of peptide nucleic acids toward electrochemical nucleic acid sensors, Analyst 146 (19) (2021) 5822–5835, https://doi.org/10.1039/d1an00765c.

[23] M. Moccia, A. Antonacci, M. Saviano, V. Caratelli, F. Arduini, V. Scognamiglio, Emerging technologies in the design of peptide nucleic acids (PNAs) based biosensors, TrAC Trends Anal Chem 132 (2020) 116062, https://doi.org/10.1016/j.trac.2020.116062.

[24] T. Rodrigues, F. Curti, Y.R. Leroux, A. Barras, Q. Pagneux, H. Happy, C. Kleber, R. Boukherroub, R. Hasler, S. Volpi, M. Careri, R. Corradini, S. Szunerits, W. Knoll, Discovery of a Peptide Nucleic Acid (PNA) aptamer for Cardiac Troponin I: substituting DNA with neutral PNA maintains picomolar affinity and improves performances for electronic sensing with graphene field-effect transistors (GFET), Nano Today 50 (2023) 101840, https://doi.org/10.1016/j.nantod.2023.101840.

[25] R. Moretta, M. Terracciano, N. Borbone, G. Oliviero, C. Schiattarella, G. Piccialli, A. P. Falanga, M. Marzano, P. Dardano, L. De Stefano, I. Rea, PNA-based graphene Oxide/Porous silicon hybrid biosensor: towards a label-free optical assay for Brugada Syndrome, Nanomaterials 10 (11) (2020) 2233, https://doi.org/10.3390/nano10112233.

[26] C. Avitabile, L. Moggio, L.D. D'Andrea, C. Pedone, A. Romanelli, Development of an efficient and low-cost protocol for the manual PNA synthesis by Fmoc chemistry, Tetrahedron Lett. 51 (29) (2010) 3716–3718, https://doi.org/10.1016/j.tetlet.2010.05.026.

[27] S.C.B. Gopinath, T. Lakshmipriya, M.K. Md Arshad, C.H. Voon, T. Adam, U. Hashim, H. Singh, S.V. Chinni, Shortening full-length aptamer by crawling base deletion – assisted by Mfold web server application, Arab J. Basic Appl. Sci. 23 (2017) 37–42, https://doi.org/10.1016/j.jaubas.2016.07.001.

[28] H. Yu, J. Zhu, G. Shen, Y. Deng, X. Geng, L. Wang, Improving aptamer performance: key factors and strategies, Mikrochim. Acta 190 (7) (2023) 255, https://doi.org/10.1007/s00604-023-05836-6.

[29] M. Terracciano, F. Fontana, A.P. Falanga, S. D'Errico, G. Torrieri, F. Greco, C. Tramontano, I. Rea, G. Piccialli, L. De Stefano, G. Oliviero, H.A. Santos, N. Borbone, Development of surface chemical strategies for synthesizing redox-responsive diatomite nanoparticles as a green platform for On-Demand intracellular release of an antisense peptide nucleic acid anticancer agent, Small 18 (41) (2022) e2204732, https://doi.org/10.1002/smll.202204732.

[30] Z. Khoshbin, M.R. Housaindokht, M. Izadyar, M.R. Bozorgmehr, A. Verdian, Recent advances in computational methods for biosensor design, Biotechnol. Bioeng. 118 (2) (2021) 555–578, https://doi.org/10.1002/bit.27618.

[31] S. Arshavsky-Graham, S.J. Ward, N. Massad-Ivanir, T. Scheper, S.M. Weiss, E. Segal, Porous silicon-based aptasensors: toward cancer protein biomarker detection, ACS Meas Sci Au 1 (2) (2021) 82–94, https://doi.org/10.1021/acsmeasuresciau.1c00019.

[32] M.G. Nolli, M. Terracciano, I. Rea, S. D'Errico, G. Placido Mineo, L. De Stefano, G. Piccialli, S. Riela, G. Oliviero, N. Borbone, Mild-temperature catalyzed hydrosilylation for simplified carbohydrate functionalization of porous silicon nanoparticles, Chem. Eur J. 31 (2) (2025) e202402818, https://doi.org/10.1002/chem.202402818.

[33] X. Miao, K. Mao, Y. Yan, Y. Pei, M.J. Sailor, L. Wu, Fabrication and performance of a superhydrophobic fluorine-modified porous silicon based on photocatalytic hydrosilylation, Micropor Mesopor Mat 330 (2022) 111561, https://doi.org/10.1016/j.micromeso.2021.111561.

[34] W. Li, Z. Liu, F. Fontana, Y. Ding, D. Liu, J.T. Hirvonen, H.A. Santos, Tailoring porous silicon for biomedical applications: from drug delivery to cancer immunotherapy, Adv Mater 30 (24) (2018) 1703740, https://doi.org/10.1002/adma.201703740.

[35] J. Jumper, R. Evans, A. Pritzel, T. Green, M. Figurnov, O. Ronneberger, K. Tunyasuvunakool, R. Bates, A. Žídek, A. Potapenko, A. Bridgland, C. Meyer, S.A. A. Kohl, A.J. Ballard, A. Cowie, B. Romera-Paredes, S. Nikolov, R. Jain, J. Adler, T. Back, S. Petersen, D. Reiman, E. Clancy, M. Zielinski, M. Steinegger, M. Pacholska, T. Berghammer, S. Bodenstein, D. Silver, O. Vinyals, A.W. Senior, K. Kavukcuoglu, P. Kohli, D. Hassabis, Highly accurate protein structure prediction with AlphaFold, Nat 596 (7873) (2021) 583–589, https://doi.org/10.1038/s41586-021-03819-2.

[36] D.A. Case, H.M. Aktulga, K. Belfon, D.S. Cerutti, G.A. Cisneros, V.W.D. Cruzeiro, N. Forouzesh, T.J. Giese, A.W. Götz, H. Gohlke, S. Izadi, K. Kasavajhala, M. C. Kaymak, E. King, T. Kurtzman, T.S. Lee, P. Li, J. Liu, T. Luchko, R. Luo, M. Manathunga, M.R. Machado, H.M. Nguyen, K.A. O'Hearn, A.V. Onufriev, F. Pan, S. Pantano, R. Qi, A. Rahnamoun, A. Risheh, S. Schott-Verdugo, A. Shajan, J. Swails, J. Wang, H. Wei, X. Wu, Y. Wu, S. Zhang, S. Zhao, Q. Zhu, T.E. Cheatham, D.R. Roe, A. Roitberg, C. Simmerling, D.M. York, M.C. Nagan, K.M. Merz, AmberTools, J. Chem. Inf. Model. 63 (20) (2023) 6183–6191, https://doi.org/10.1021/acs.jcim.3c01153.

[37] A.P. Falanga, I. Piccialli, F. Greco, S. D'Errico, M.G. Nolli, N. Borbone, G. Oliviero, G.N. Roviello, Nanostructural modulation of g-quadruplex DNA in neurodegeneration: orotate interaction revealed through experimental and computational approaches, J. Neurochem. 169 (1) (2025) e16296, https://doi.org/10.1111/jnc.16296.

[38] B. Ropii, M. Bethasari, I. Anshori, A.P. Koesoema, W. Shalannanda, A. Satriawan, C. Setianingsih, M.R. Akbar, R. Aditama, F. Fahmi, E. Sutanto, M. Yazid, M. Aziz, The molecular interaction of six single-stranded DNA aptamers to Cardiac Troponin I revealed by docking and molecular dynamics simulation, PLoS One 19 (5) (2024) e0302475, https://doi.org/10.1371/journal.pone.0302475.

[39] S. Huang, X. Zou, An iterative knowledge-based scoring function for protein–protein recognition, Proteins 72 (2) (2008) 557–579, https://doi.org/10.1002/prot.21949.

[40] J.A. Maier, C. Martinez, K. Kasavajhala, L. Wickstrom, K.E. Hauser, C. Simmerling, Ff14SB: improving the accuracy of protein side chain and backbone parameters from Ff99SB, J Chem Theory Comput 11 (8) (2015) 3696–3713, https://doi.org/10.1021/acs.jctc.5b00255.

[41] J.M. Sanders, M.E. Wampole, C.-P.P. Chen, D. Sethi, A. Singh, F.-Y.Y. Dupradeau, F. Wang, B.D. Gray, M.L. Thakur, E. Wickstrom, Effects of hypoxanthine substitution in peptide nucleic acids targeting KRAS2 oncogenic MRNA molecules: theory and experiment, J. Phys. Chem. B 117 (39) (2013) 11584–11595, https://doi.org/10.1021/jp4064966.

[42] W.L. Jorgensen, J. Chandrasekhar, J.D. Madura, R.W. Impey, M.L. Klein, Comparison of simple potential functions for simulating liquid water, J. Chem. Phys. 79 (2) (1983) 926–935, https://doi.org/10.1063/1.445869.

[43] H.J.C. Berendsen, J.P.M. Postma, W.F. Van Gunsteren, A. Dinola, J.R. Haak, Molecular dynamics with coupling to an external Bath, J. Chem. Phys. 81 (8) (1984) 3684–3690, https://doi.org/10.1063/1.448118.

[44] T. Darden, D. York, L. Pedersen, Particle mesh ewald: an N·log(N) method for ewald Sums in large systems, J. Chem. Phys. 98 (12) (1993) 10089–10092, https://doi.org/10.1063/1.464397.

[45] J.-P. Ryckaert, G. Ciccotti, H.J.C. Berendsen, Numerical integration of the Cartesian equations of motion of a system with constraints: molecular dynamics of n-Alkanes, J. Comput. Phys. 23 (3) (1977) 327–341, https://doi.org/10.1016/0021-9991(77)90098-5.

[46] C.A. Schneider, W.S. Rasband, K.W. Eliceiri, NIH image to ImageJ: 25 years of image analysis, Nat. Methods 9 (7) (2012) 671–675, https://doi.org/10.1038/nmeth.2089.

[47] C. De Rosa, F. Morgillo, L. Amato, F. Iommelli, V. De Rosa, V. Tirino, F. Papaccio, C. Tuccillo, G. Di Guida, D.M. D'Angiolella, A. Di Liello, S. Zappavigna, M. Caraglia, A. Gambardella, V. Nardone, K. Ramkumar, Q. Wang, J. Wang, F. De Vita, D. Ciardiello, E. Martinelli, T. Troiani, S. Napolitano, G. Martini, A. Servetto, L.A. Byers, F. Ciardiello, C.M. Della Corte, DNA-PK inhibition sustains the Antitumor innate immune response in small cell lung cancer, iScience 28 (3) (2025) 111943, https://doi.org/10.1016/j.isci.2025.111943.

[48] M. Terracciano, I. Rea, N. Borbone, R. Moretta, G. Oliviero, G. Piccialli, L. De Stefano, Porous silicon-based aptasensors: the next generation of label-free devices for health monitoring, Molecules 24 (12) (2019) 2216, https://doi.org/10.3390/molecules24122216.

[49] C. Lai, Z. Xiang, Investigation the effect of porosity on corrosion of macroporous silicon in 1.0M sodium hydroxide solution using weight loss measurements, electrochemical methods and scanning electron microscope, Corros. Sci. 99 (2015) 178–184, https://doi.org/10.1016/j.corsci.2015.06.025.

[50] C. Lai, X. Li, D. Zhang, Z. Xiang, W. Yang, X. Guo, Fabrication and corrosion behavior of fresh porous silicon in sodium hydroxide solution, Mater. Chem. Phys. 144 (3) (2014) 355–360, https://doi.org/10.1016/j.matchemphys.2014.01.002.

[51] T.I. Rodrigues, F. Curti, Y.R. Leroux, A. Barras, Q. Pagneux, H. Happy, C. Kleber, R. Boukherroub, R. Hasler, S. Volpi, M. Careri, R. Corradini, S. Szunerits, W. Knoll, Discovery of a Peptide Nucleic Acid (PNA) aptamer for Cardiac Troponin I: substituting DNA with neutral PNA maintains picomolar affinity and improves performances for electronic sensing with graphene field-effect transistors (gFET), Nano Today 50 (2023) 101840, https://doi.org/10.1016/j.nantod.2023.101840.

[52] M. Negahdary, M. Behjati-Ardakani, H. Heli, N. Sattarahmady, A cardiac troponin T biosensor based on aptamer self-assembling on gold, Int. J. Mol. Cell. Med. 8 (4) (2019) 271, https://doi.org/10.22088/IJMCM.BUMS.8.4.271.

[53] H. Yu, O. Alkhamis, J. Canoura, Y. Liu, Y. Xiao, Advances and challenges in small-molecule DNA aptamer isolation, characterization, and sensor development, Angew. Chem. Int. Ed. 60 (31) (2021) 16800–16823, https://doi.org/10.1002/anie.202008663.

[54] N. Brodyagin, M. Katkevics, V. Kotikam, C.A. Ryan, E. Rozners, Chemical approaches to discover the full potential of peptide nucleic acids in biomedical applications, Beilstein J. Org. Chem. 17 (2021) 1641–1688, https://doi.org/10.3762/bjoc.17.116.

[55] A. Gamble Jarvi, A. Sargun, X. Bogetti, J. Wang, C. Achim, S. Saxena, Development of Cu2+-Based distance methods and force field parameters for the determination of PNA conformations and dynamics by EPR and MD simulations, J. Phys. Chem. B 124 (35) (2020) 7544–7556, https://doi.org/10.1021/acs.jpcb.0c05509.

[56] P. Weroński, Y. Jiang, S. Rasmussen, Molecular dynamics study of small PNA molecules in lipid-water system, Biophys. J. 92 (9) (2007) 3081–3091, https://doi.org/10.1529/biophysj.106.097352.

[57] R.D. González, A.T.P. Carvalho, Papain-Mediated conjugation of peptide nucleic acids to delivery peptides: a density functional Theory/Molecular mechanics metadynamics study in aqueous and organic solvent, J. Phys. Chem. B 128 (31) (2024) 7500–7512, https://doi.org/10.1021/acs.jpcb.4c02294.

[58] M.D. Verona, V. Verdolino, F. Palazzesi, R. Corradini, Focus on PNA flexibility and RNA binding using molecular dynamics and metadynamics, Sci. Rep. 7 (1) (2017) 42799, https://doi.org/10.1038/srep42799.

[59] I. Autiero, M. Saviano, E. Langella, Conformational studies of chiral D-Lys-PNA and achiral PNA system in binding with DNA or RNA through a molecular dynamics approach, Eur. J. Med. Chem. 91 (2015) 109–117, https://doi.org/10.1016/j.ejmech.2014.08.015.

[60] M. Falanga, C. Cortesi, A. Chiaravalloti, A.D. Monte, C. Tomasi, C. Corsi, A digital twin approach for stroke risk assessment in atrial fibrillation patients, Heliyon 10 (20) (2024) e39527, https://doi.org/10.1016/j.heliyon.2024.e39527.

[61] M. Moccia, F.A. Mercurio, E. Langella, V. Piacenti, M. Leone, M.F.A. Adamo, M. Saviano, Structural insights on tiny Peptide Nucleic Acid (PNA) analogues of MiRNA-34a: an in silico and experimental integrated approach, Front. Chem. 8 (2020) 568675, https://doi.org/10.3389/fchem.2020.568575.

[62] A. Bartocci, E. Dumont, Situating the phosphonated calixarene–cytochrome C association by molecular dynamics simulations, J. Chem. Phys. 160 (10) (2024) 105101, https://doi.org/10.1063/5.0198522.

[63] A. Bartocci, G. Pereira, M. Cecchini, E. Dumont, Capturing the recognition dynamics of Para-Sulfonato-Calix[4]Arenes by cytochrome c: toward a quantitative free energy assessment, J. Chem. Inf. Model. 62 (24) (2022) 6739–6748, https://doi.org/10.1021/acs.jcim.2c00483.

[64] A.P. Falanga, M. Cremonini, A. Bartocci, M.G. Nolli, M. Terracciano, S. Volpi, E. Dumont, G. Piccialli, A. Casnati, F. Sansone, N. Borbone, G. Oliviero, Calixarenes meet (TG4T)4 G-Quadruplex: exploring reciprocal interactions to develop innovative biotechnological applications, Int. J. Biol. Macromol. 305 (2025) 141331, https://doi.org/10.1016/j.ijbiomac.2025.141331.

[65] S. Denis-Quanquin, A. Bartocci, F. Szczepaniak, F. Riobé, O. Maury, E. Dumont, N. Giraud, Capturing the dynamic association between a tris-dipicolinate lanthanide complex and a decapeptide: a combined paramagnetic NMR and molecular dynamics exploration, Phys. Chem. Chem. Phys. 23 (19) (2021) 11224–11232, https://doi.org/10.1039/D0CP06570F.

[66] Z. Mokhtari, H. Khajehsharifi, S. Hashemnia, S. Shahrokhian, Predicting the cardiac troponin I (CTnl) Aptamer/Methylene blue configuration using computational modeling studies: a screening search method for constructing aptasensors, ChemistrySelect 5 (35) (2020) 10958–10969, https://doi.org/10.1002/slct.202001780.

[67] H. Begum, P. Murugesan, A.D. Tangutur, Western blotting: a powerful staple in scientific and biomedical research, Biotechniques 73 (1) (2022) 58–69, https://doi.org/10.2144/btn-2022-0003.

[68] I.A. Katrukha, N.S. Riabkova, A.E. Kogan, A.V. Vylegzhanina, K. Sh Mukharyamova, A.P. Bogomolova, A.I. Zabolotskii, E.V. Koshkina, A. V. Bereznikova, A.G. Katrukha, Fragmentation of human cardiac Troponin T after acute myocardial infarction, Clin. Chim. Acta 542 (2023) 117281, https://doi.org/10.1016/j.cca.2023.117281.

[69] F. Fan, L. Fang, X.L. Moore, X. Xie, X.J. Du, D.A. White, J. O'Brien, H. Thomson, J. Wang, H.G. Schneider, A. Ellims, T.W. Barber, A.M. Dart, Plasma macrophage migration inhibitor factor is elevated in response to myocardial ischemia, J. Am. Heart Assoc. 5 (7) (2016) e003128, https://doi.org/10.1161/JAHA.115.003128.

[70] M. Terracciano, I. Rea, L. De Stefano, I. Rendina, G. Oliviero, F. Nici, S. D'Errico, G. Piccialli, N. Borbone, Synthesis of mixed-sequence oligonucleotides on mesoporous silicon: chemical strategies and material stability, Nanoscale Res. Lett. 9 (1) (2014) 1–9, https://doi.org/10.1186/1556-276X-9-317.

[71] M. Terracciano, L. De Stefano, N. Borbone, J. Politi, G. Oliviero, F. Nici, M. Casalino, G. Piccialli, P. Dardano, M. Varra, I. Rea, Solid phase synthesis of a thrombin binding aptamer on macroporous silica for Label free optical quantification of thrombin, RSC Adv. 6 (90) (2016) 86762–86769, https://doi.org/10.1039/c6ra18401d.

[72] U.C. Hasar, I.Y. Ozbek, B. Cavusoglu, T. Karacali, H. Efeoglu, M. Ertugrul, J. J. Barroso, Characterization of porous silicon fabry–pérot optical sensors for reflectivity and transmittivity measurements, IEEE J Sel Top Quantum Electron 21 (4) (2015) 174–183, https://doi.org/10.1109/JSTQE.2014.2365583.

[73] K. Awawdeh, M.A. Buttkewitz, J. Bahnemann, E. Segal, Enhancing the performance of porous silicon biosensors: the interplay of nanostructure design and microfluidic integration, Microsyst Nanoeng 10 (1) (2024) 100, https://doi.org/10.1038/s41378-024-00738-w.

[74] T.C. Tsai, C.W. Liu, Y.C. Wu, N.A.P. Ondevilla, M. Osawa, H.C. Chang, In situ Study of EDC/NHS immobilization on gold surface based on attenuated total reflection surface-enhanced infrared absorption spectroscopy (ATR-SEIRAS), Colloids Surf. B Biointerfaces 175 (2019) 300–305, https://doi.org/10.1016/j.colsurfb.2018.12.009.

[75] C. Lai, Z. Xiang, Investigation the effect of porosity on corrosion of macroporous silicon in 1.0M sodium hydroxide solution using weight loss measurements, electrochemical methods and scanning electron microscope, Corros. Sci. 99 (2015) 178–184, https://doi.org/10.1016/j.corsci.2015.06.025.

[76] N.L. Fry, G.R. Boss, M.J. Sailor, Oxidation-Induced trapping of drugs in porous silicon microparticles, Chem. Mater. 26 (8) (2014) 2758–2764, https://doi.org/10.1021/cm500797b.

[77] A.M. Chaulin, The metabolic pathway of cardiac troponins release: mechanisms and diagnostic role, Cardiol Res 13 (4) (2022) 190–205, https://doi.org/10.14740/cr1351.

[78] H. Haybar, M. Jalali, K. Zibara, Z. Zayeri, Mechanisms and biomarkers to detect chemotherapy-induced cardiotoxicity, Clin. Cancer Investig. J. 6 (5) (2017) 207, https://doi.org/10.4103/ccij.ccij_47_17.

[79] G. Tsaknis, I. Tsangaris, I. Ikonomidis, A. Tsantes, Clinical usefulness of novel serum and imaging biomarkers in risk stratification of patients with stable angina, Dis. Markers 2014 (1) (2014) 831364, https://doi.org/10.1155/2014/831364.